

Development of a Miniature Double Focusing Mass Spectrograph Using a Focal Plane Detector

Masaru NISHIGUCHI,^{1*} Michisato TOYODA,¹ Morio ISHIHARA,¹ Makiko OHTAKE,²
Takamitsu SUGIHARA,³ and Itsuo KATAKUSE¹

¹ *Department of Physics, Graduate School of Science, Osaka University, Toyonaka, JAPAN*

² *Research Division for Planetary Science, Institute of Space and Astronautical Science, Japan Aerospace Exploration Agency, Sagami-hara, JAPAN*

³ *Center for Deep Earth Exploration, Japan Agency for Marine-Earth Science and Technology, Yokohama, JAPAN*

A miniature mass spectrograph was newly designed and constructed as a prototype model for future lunar or planetary explorations. The ion optical system was newly designed based on Mattauch–Herzog geometry. The mass spectrograph employs a focal plane detector consisting of a microchannel plate (MCP), a phosphor layer, a fiber-optic plate (FOP) and a charge-coupled device (CCD). The 2D and 1D spectra of the residual gases, krypton and neon were observed in preliminary experiments. The mass resolution of 130 was achieved experimentally, and this was in good agreement with the simulation based on the transfer matrix method. The experimental value of the detectable m/z range was also consistent with the calculated version. Moreover, stable isotopes of Kr and Ne were observed without saturation of the detector. A dynamic range of 300 was achieved.

(Received September 5, 2005; Accepted October 19, 2005)

1. Introduction

The analysis of the atmosphere and surface substances in lunar and planetary explorations is of interest for space science. In particular, measurements of the elemental composition and the isotope ratio of surface substances provide basic information on the origin and evolution of the planets. Mass spectrometry is obviously the most suitable method for these purposes, so mass spectrometers have often been employed in past and present space missions. For example, two mass spectrometers were on board in the Viking mission: one was a double focusing mass spectrometer using Mattauch–Herzog geometry for analysis of the Martian atmosphere¹⁾ and the other was a gas chromatograph(GC)–mass spectrometer employing a double focusing analyzer using Nier–Johnson geometry for the measurement of organic compounds in the surface soil.²⁾ Quadrupole mass spectrometers were also carried on several space probes to analyze the atmosphere: the Huygens Probe in the Cassini–Huygens mission³⁾ and others.^{4), 5)} An instrument for space explorations must feature reduced size, weight and electric power consumption. Magnetic sector, quadrupole or time-of-flight (TOF) mass spectrometers are generally employed for space exploration. A magnetic sector analyzer is not amenable to weight reduction due to its heavy magnet. On the other hand, quadrupole and TOF analyzers have good potential for weight reduction because they

consist of only electrodes. Magnetic analyzers, on the other hand, provide a large dynamic range. If the exploration target is near the Earth, *e.g.*, lunar or Mars exploration, the weight of the instrument is less crucial. In that case, a magnetic sector analyzer may provide the advantage of good quantitative performance.

When mass spectra are obtained by scanning the magnetic field strength or the accelerating voltage of ions in a magnetic sector analyzer, most of the ions cannot pass through the collector slit and thus are not detected. If all the ions that pass through the analyzer are detected simultaneously, the detection efficiency can be drastically improved. Quantitative performance, furthermore, can also be improved by simultaneous detection because time-dependent fluctuations can be eliminated. For these reasons, a mass spectrograph that employs a magnetic sector analyzer and a focal plane detector⁶⁾ is ideally suited for trace and quantitative analysis. For the same reasons, a mass spectrometer employing multiple collectors^{7), 8)} is also effective. Several mass spectrographs equipped with focal plane detectors have been developed since the 1970.^{9)–13)} For example, Giffin *et al.*⁹⁾ applied a focal plane detector comprising a microchannel plate (MCP), a phosphor screen, a fiber-optic image dissector and a vidicon camera system to a mass spectrograph with Mattauch–Herzog geometry.^{14), 15)} Murphy and Mauersberger¹¹⁾ developed an MCP detector system that consists of an MCP, a phosphor layer on a fiber-optic bundle and a photodiode array, and operated the detector in ion counting mode for a mass spectrograph with Mattauch–Herzog geometry. Burgoyne *et al.*¹²⁾ also employed an MCP with an active phosphor for a mass spectrograph with Mattauch–Herzog geometry. They

* Correspondence to: Masaru NISHIGUCHI, *Department of Physics, Graduate School of Science, Osaka University, 1-1 Machikaneyama, Toyonaka, Osaka 560-0043, JAPAN*, e-mail: nishiguchi@mass.phys.sci.osaka-u.ac.jp

detected the phosphor images using a 1.32-cm charge-coupled device (CCD). Yurimoto *et al.* employed a stacked CMOS-type active pixel sensor for two-dimensional isotope ratio imaging in secondary ion mass spectrometry.¹⁶⁾

Thus, several types of devices are used as focal plane detectors.¹⁷⁾ An MCP is the most often used device as a focal plane detector.⁶⁾ Although an MCP can provide a cloud of electrons, a system, which can detect these electrons and retain the spatial information, is necessary for a mass spectrograph. For this reason, an MCP is generally combined with two types of electron-detecting systems: one is a photon detector, *e.g.*, a CCD or a photodiode array with a phosphor screen, and the other is a multi-anode detector. In recent years, thanks to progress in semiconductor technology, large CCDs with high spatial resolution have become available at comparatively low cost.

As described above, a double focusing mass spectrograph is suited for space exploration near the Earth due to its high sensitivity and good quantitative performance. We have therefore developed a miniature double focusing mass spectrograph for future lunar explorations.¹⁸⁾ We newly designed an ion optical system for use in the double focusing mass spectrograph equipped with a focal plane detector. The focal plane detector is the most important part of the mass spectrograph since the performance of the instrument depends on the detector's performance. The prototype instrument employed an MCP-based position sensitive detector. In this focal plane detector, the MCP is combined with a phosphor layer and a CCD. The size of the active area of the focal plane detector is about $5\text{ cm} \times 1\text{ cm}$. Our target is to achieve a highly sensitive and good quantitative performance by the simultaneous detection of ions over a wide mass range.

In this paper, the ion optical system and details of the instrument are described. We also report on the preliminary experiments for the evaluation of the instrument.

2. Experimental, Results, and Discussion

2.1 Ion optics

The typical ion optical system for the double focusing mass analyzers uses either Mattauch–Herzog geometry^{14), 15)} or Nier–Johnson geometry.¹⁹⁾ Nier–Johnson geometry provides only one double focusing point, *i.e.* the energy focal plane and the angular focal plane intersect at one point. On the other hand, Mattauch–Herzog geometry provides the double focusing on a straight line at the exit of the magnet. Double focusing points arranged in a straight line are ideal for the use of a focal plane detector. We have newly designed an ion optical system based on Mattauch–Herzog geometry.

As already stated, instruments for space exploration need to be small and light. We have assumed lunar surface exploration with the mass spectrograph loaded on a rover. The measuring objects are the ice in the poles and noble gases in the low mass range from He to Ar. The required specifications of the mass spectrograph for loading on a rover are as follows¹⁸⁾: the size of the mass analyzer must be less than $200\text{ mm} \times 150\text{ mm} \times 100\text{ mm}$; the weight must be less than 3 kg; the mass range of the measurements is from 1 u to 50 u. And, the

target of the dynamic range is 10^4 required for the measurement of the isotope ratios of Ar.

The magnet is the most important part of the instrument, since it is the heaviest part, and the detectable range of mass to charge ratio (m/z) depends on the size of the magnet. Here, the detectable m/z range is defined as the ratio of the maximal to the minimal observable m/z , and is expressed in terms of the maximal radius r_{max} and the minimal radius r_{min} of the trajectories in the magnetic field as $(r_{\text{max}}/r_{\text{min}})^2$; the maximal radius should be increased, or the minimal radius should be decreased to achieve a wide range of detectable m/z . The maximal radius, however, directly depends on the magnet size; thus, it is limited. On the other hand, the minimal radius is also limited. Because the distribution of the magnetic field strength would not be homogeneous in the region of the magnet fringe, the minimal radius must be sufficiently larger than the gap width between the pole pieces. In the prototype instrument, the maximal radius and the minimal radius are 75 mm and 25 mm, respectively. In this design, the detectable m/z range of 7 is sufficiently achieved. If it is required to detect from 1 u to 49 u, the observed mass region can be altered by switching the accelerating voltage and the field strength of the electrostatic sector. When low mass ions from 1 u to 7 u are observed at a high accelerating voltage V_h , the high mass ions from 7 u to 49 u can be observed at a low accelerating voltage $V_l = V_h/7$.

We employed a spherical electrostatic sector in the ion optical system. The spherical electric field exerts focusing actions in both the vertical and horizontal directions and contributes to achieving high transmission in the magnetic sector. The mean radius of the spherical electrostatic sector is 50 mm.

We considered the following two conditions in the design of the ion optical parameters: the ion beams must be parallel in the drift space between the electrostatic sector and the magnetic sector, and both the energy and angular focal planes must be placed at a distance from the exit of the magnet. The first condition is theoretically required to realize a straight line for double focusing.¹⁵⁾ This condition can be easily fulfilled by adjusting the length of the first drift space between the ion source and the electrostatic sector. The second condition is needed to mount a focal plane detector on the mass analyzer. In the Mattauch–Herzog geometry, the focal planes are placed at the exit of the magnet. However, to install an MCP-based position sensitive detector, it is desirable that the focal planes be at a distance from the exit of the magnet. The fringing field of the magnet will exert a defocusing action in the horizontal direction if the inclination angle between the incident normal of the field boundary and the optical axis is positive.²⁰⁾ Therefore, the second condition can be fulfilled with a positive inclination angle at the magnet entrance.

The design of the ion optical system was carried out with the computer programs “TRIO”²¹⁾ and “TRIO-DRAW”²²⁾ based on the transfer matrix method.²³⁾⁻²⁵⁾ The schematic drawing of the ion optical system is shown in Fig. 1. The deflection angle of the electrostatic sector is 60° and the gap between the electrodes is 10

Table 1. The Ion Optical Parameters and the Elements of the Transfer Matrix

Drift space	DL1=0.0345
Toroidal ESA entrance	RO1=0.0000, GAP=0.0050, NE1=2
Toroidal ESA	AE=0.0500, WE=60.00, C1=1.0000, C2=-1.0000
Toroidal ESA exit	RO2=0.0000, GAP=0.0050, NE2=2
Drift space	DL2=0.0450
Deflection is in reverse sense	
Sector magnet entrance	EP1=48.71, RO1=0.0000, GAP=0.0050, NM1=2
Sector magnet	AM=0.0500, WM=74.73, N1=0.0000, N2=0.0000
Sector magnet exit	EP2=-52.63, RO2=0.0000, GAP=0.0050, NM2=2
Deflection is in reverse sense	
Drift space	DL3=0.0269

Transfer matrix relating to the region from the ion source to the ESA exit:

	x	α	γ	δ
x	0.5525	0.0625	0.0000	0.0250
α	-16.00	0.0000	0.0000	0.8937

Transfer matrix of the whole system:

	x	α	γ	δ	xx	$x\alpha$	$x\gamma$	$x\delta$	$\alpha\alpha$
x	-0.3267	0.0000	-0.01825	0.0000	-38.42	5.313	-1.211	8.554	-0.3034
α	27.60	-3.061	0.00689	-4.271	1677	269.7	-6.080	-121.9	0.7392
	$\alpha\gamma$	$\alpha\delta$	$\gamma\gamma$	$\gamma\delta$	$\delta\delta$	yy	$y\beta$	$\beta\beta$	
x	0.1160	-0.6745	0.00435	0.1619	-0.4602	17.09	-0.04869	-0.00011	
α	1.552	-23.11	-0.00359	1.727	-3.706	-1378	-205.3	0.7713	

 Table 2. The Elements of $(x|\alpha)$ and $(x|\delta)$ for Several Mean Radii in the Magnetic Field

r_m (mm)	DL3 (m)	$(x \alpha)$	$(x \delta)$
25	0.0122	-0.0002	0.0000
30	0.0153	-0.0002	0.0000
35	0.0183	-0.0001	0.0000
40	0.0212	-0.0001	0.0000
45	0.0241	0.0000	0.0000
50	0.0269	0.0000	0.0000
55	0.0298	0.0000	0.0000
60	0.0326	0.0000	0.0000
65	0.0355	0.0001	0.0000
70	0.0383	0.0001	0.0000
75	0.0411	0.0001	0.0000

mm. The inclination angle at the magnet entrance is 48.71° . The deflection angle of the magnetic sector is 74.73° and the gap between the pole pieces is 4 mm. The required size of the focal plane detector depends on the radius and the deflection angle of the magnet. If the maximal radius and the minimal radius are set at 66 mm and 25 mm, respectively, to achieve the detectable m/z range of 7, the required detector size is 70 mm.

The ion optical parameters, the elements of transfer matrix relating to the region from the ion source to the exit of the electrostatic sector, and those of the whole system are shown in Table 1. The definitions of the ion optical parameters are presented in ref. 21. Here x and α denote the positional and angular deviations of the arbitrary trajectories in the horizontal direction, and y and β denote the same ones in the vertical direction. They are defined with respect to the optical axis. The unit of x and y is meter, and the unit of α and β is radian.

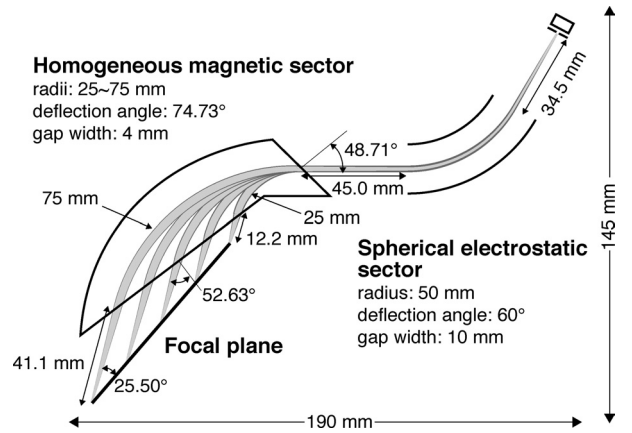


Fig. 1. Schematic drawing of the newly designed ion optical system.

The mass and energy deviations, γ and δ , are defined as

$$m/e = (m_0/e_0)(1 + \gamma), \quad U/e = (U_0/e_0)(1 + \delta) \quad (1)$$

where m , e , U are the mass, charge, and energy of an arbitrary ion and m_0 , e_0 , U_0 are those of a reference ion. As expressed in Eq. (1), γ and δ are dimensionless parameters. Hereinafter, each element of the transfer matrix is denoted by row and column parameters, e.g., the element in row x and in column α is denoted as $(x|\alpha)$. The element of $(\alpha|\alpha)$ in the transfer matrix relating to the region from the ion source to the electrostatic sector is equal to zero. This indicates that the angle of an ion beam is independent of its initial angle, i.e., the ion beams run parallel in the drift space between the electrostatic sector and the magnetic sector. The elements of $(x|\alpha)$ and $(x|\delta)$ in the transfer matrix of the whole system are equal to zero. This indicates that the

double focusing is satisfied in this ion optical system. The elements of $(x|\alpha)$ and $(x|\delta)$ for several mean radii of ion trajectories from 25 mm to 75 mm at 5 mm intervals in the magnetic field are shown in Table 2. The second column of the table shows the length of the last drift space between the magnetic sector and the detector. Double focusing is satisfactorily achieved for all mean radii in the magnetic field, and the double focusing points are in a straight line, as shown in Fig. 1. The ion trajectories with the mean radii of 50 mm in the magnetic field were simulated by “TRIO-DRAW,” as shown in Fig. 2. Figure 2(a) shows the ion trajectories in the x direction and Fig. 2(b) shows those in the y direction. We can confirm the double focusing is achieved in the x direction in Fig. 2(a). And in Fig. 2(b), ion trajectories are compressed in the y direction before entering the magnetic sector. This indicates the spherical electrostatic sector effectively contributes to a high transmission in the magnetic sector.

As mentioned above, this ion optical system has the following features: the double focusing for the use of a focal plane detector is fulfilled in a straight line placed at a distance from the exit of the magnet; a high transmission can be achieved by employing the spherical electrostatic sector.

2.2 Instrument

A prototype model employing the newly designed ion optical system was constructed. The instrument is equipped with an EI ion source, a spherical electrostatic sector, a homogeneous magnetic sector and a focal plane detector using a CCD. This instrument can detect ions over a wide mass range simultaneously by employing the new ion optical system and equipping the focal plane detector whose size is about 5 cm. The

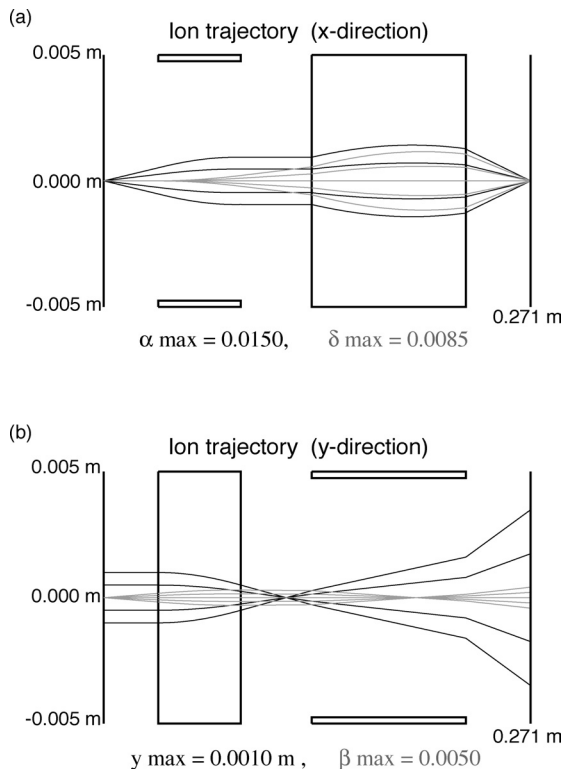


Fig. 2. Ion trajectories simulated by “TRIO-DRAW.” (a) x -direction; (b) y -direction.

details of the focal plane detector are presented in subsection 2.2.2. The technical drawing and a photograph of this instrument are shown in Figs. 3 and 4. The instrument is set in a circular vacuum chamber whose diameter is 40 cm, and the mass analyzer is fixed on a base plate whose size is about 20 cm \times 20 cm. The focal plane detector is fixed to a movable stage. The vacuum chamber is evacuated with a turbomolecular pump (TMP 280G, SHIMADZU CORPORATION, Kyoto, Japan). The vacuum pressure is measured with an ionization gauge (GI-TL2, ULVAC, Inc., Kanagawa, Japan) attached at the side of the vacuum chamber. The base pressure is maintained at about 4×10^{-4} Pa.

2.2.1 Ion source and mass analyzer The EI ion source is the same one as used for the JMS-HX110 (JEOL, Tokyo, Japan). The development of a small and light ion source is also important in space exploration. A reliable ion source is, however, needed to evaluate the ion optical properties. Thus, the commercially available ion source was employed in the prototype instrument.

The mean radius, the gap width of the electrodes, the deflection angle and the height of the spherical electrostatic sector are 50 mm, 10 mm, 60° and 40 mm, respectively. If the accelerating voltage of ions is V_a , the theoretical voltage applied to the electrodes is $\pm 0.1980 V_a$. The α -slit is placed at the entrance of the electrostatic sector.

To save power consumption, the magnetic field is generated by a permanent magnet. A schematic drawing of the magnetic circuit is shown in Fig. 5. The pole pieces with the thickness of 8 mm were designed to achieve a sufficient uniformity of magnetic field. The thickness of the permanent magnet materials is 4 mm. The gap width between the pole faces is 4 mm. Low-carbon steel SS400 (JIS G3101) is used for the pole piece and the yoke. The permanent magnet is a sintered Nd-Fe-B magnet (NEOMAX 39SH, NEOMAX Co., Ltd., Osaka, Japan). Since the magnetic material is porous, the surface of the magnet is coated with TiN. This coating prevents adsorbed gases flowing out from

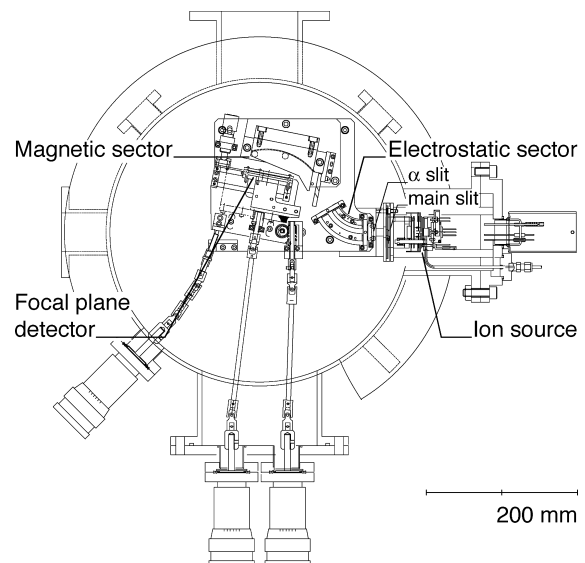


Fig. 3. Technical drawing of the prototype instrument.

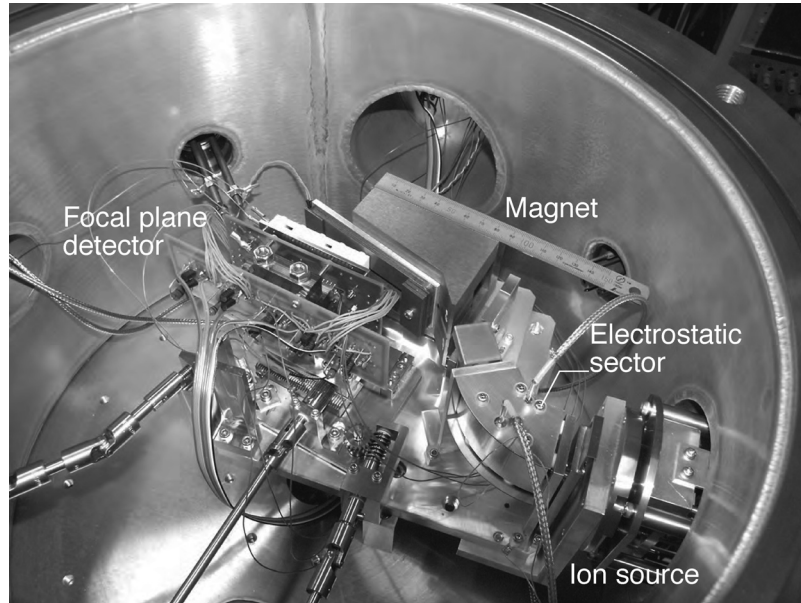


Fig. 4. Prototype instrument in the vacuum chamber.

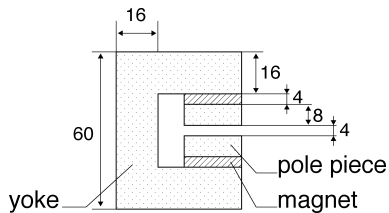


Fig. 5. Schematic drawing of the magnetic circuit.

the magnet. The magnetic flux density is 0.576 T. When ions of m/z 4 are accelerated to 10 keV, the mean radius of the ion trajectory in the magnetic field is 50 mm.

2.2.2 Focal plane detector The instrument employs an MCP-based position sensitive detector. The detector consists of an MCP, a phosphor layer on a fiber-optic plate (FOP) and a CCD. The schematic drawing of the focal plane detector is shown in Fig. 6. Ion beams entering the channels of the MCP are converted and amplified to electron clouds by the MCP. The MCP also retains the spatial information of the profile of the ion beam. These electrons are accelerated to the phos-

phor layer and converted into photons. These photons then pass through the FOP and are detected by the CCD.

An assembly (F4301-04, Hamamatsu Photonics, Shizuoka, Japan) comprising an MCP, a phosphor layer and a FOP is used for the detector. The active area of the MCP is $55\text{ mm} \times 8\text{ mm}$ and the channel diameter is $12\text{ }\mu\text{m}$. The MCP is composed of two stages and the typical gain is over 10^6 if the voltage applied to the MCP is 2.0 kV. The front surface of the MCP is grounded. The type of phosphor is P46, and the typical wavelength and the decay time are 530 nm and 300 ns, respectively. The CCD is a front-illuminated type CCD (S7175F, Hamamatsu Photonics, Shizuoka, Japan). The CCD is a full frame transfer type (FFT). The number of active pixels is 1024 (horizontal) \times 128 (vertical), each pixel is $48\text{ }\mu\text{m} \times 48\text{ }\mu\text{m}$, and the active area is $49.152\text{ mm} \times 6.144\text{ mm}$.

The FFT-CCD is normally used in conjunction with an external shutter mechanism to ensure that no light enters the CCD while the signal charges are being transferred from the imaging section. A pulsed voltage is applied to the deflection electrode in the ion source to

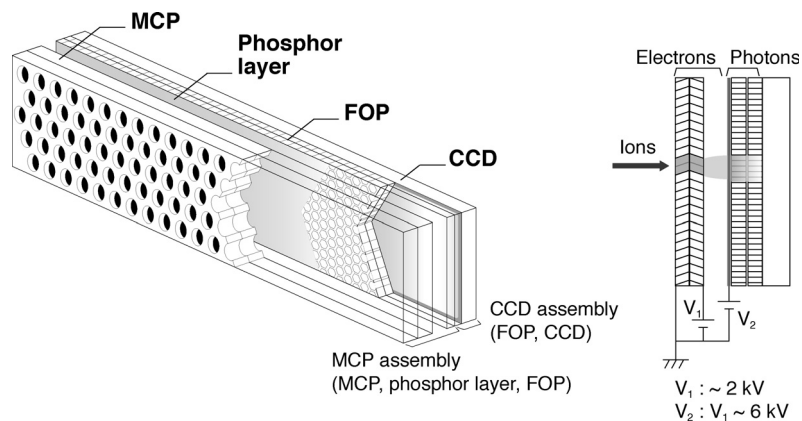


Fig. 6. Schematic drawing of the focal plane detector.

prevent the ion beam entering the detector while the signal charges are being transferred inside the CCD. The CCD can be operated in two modes: line binning and pixel binning. In line binning, the signal charges in the vertical shift register are accumulated in the horizontal direction and the output data comprises a one-dimensional stream of 1024 channels. In the pixel binning operation, the signal charges of all pixels are sent to the output section one after another and the output data comprises two-dimensional data of 1024×128 channels. The schematic drawing of the data acquisition system is shown in Fig. 7. The timing signals for controlling the CCD and the shutter mechanism are supplied by a digital I/O board (PCI-2472C, Interface, Hiroshima, Japan). The clock frequency of the signal charge transfer is 100 kHz. Thus, the frame rate in line binning is about 100 frames per second (fps), and that in pixel binning is about 1 fps. The analog signal from the CCD is first amplified by the preamplifier installed near the CCD. The block diagram of the CCD control system and the shutter mechanism in pixel binning is shown in Fig. 8. The output signal of the preamplifier is then amplified by the main amplifier, and the output of the main amplifier is acquired as a digital signal *via* a 12-bit A/D board (PCI-3163, Interface, Hiroshima, Japan).

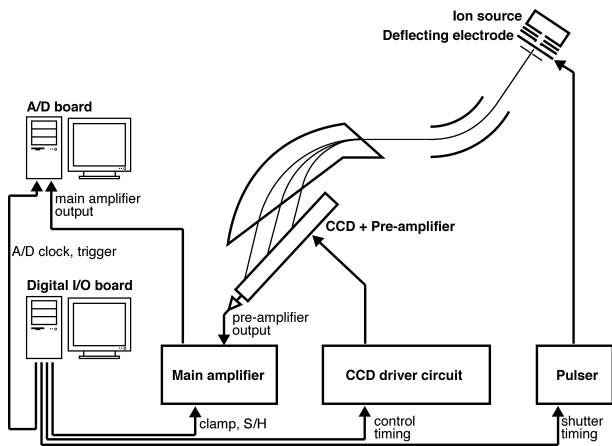


Fig. 7. Data acquisition and CCD control system.

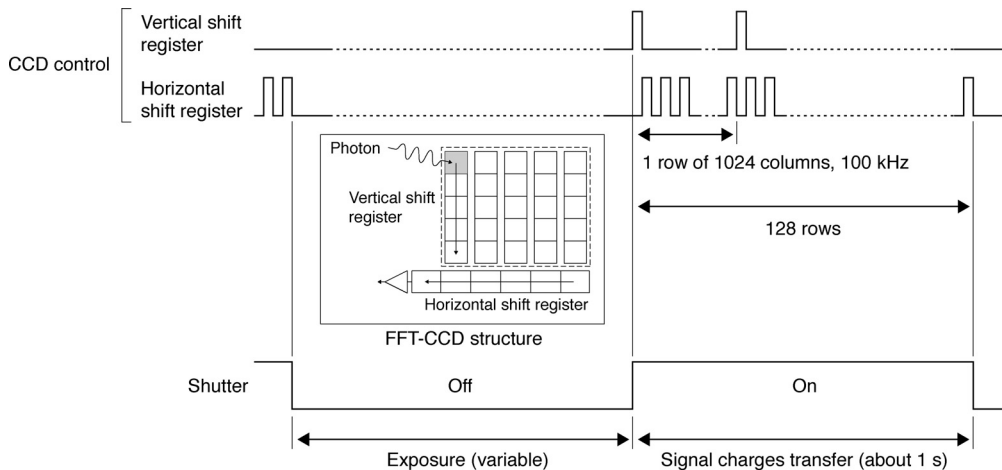


Fig. 8. Timing chart of the CCD control system and shutter mechanism in pixel binning.

2.3 2D and 1D spectra

For the investigation of the ion optical system and the detecting system, the 2D and 1D spectra of the residual gases were observed. The 2D and 1D spectra of the residual gases are shown in Figs. 9 and 10, respectively. The experimental conditions were as follows: the width and the height of the main slit were 0.25 mm and 2.0 mm; the width and the height of the α -slit were 0.5 mm and 3.0 mm; the accelerating voltage of the ions was 2200 V; the voltage applied to the electrostatic sector was ± 435.6 V; the electron energy and the electron current for the ionization were 70 eV and $250 \mu\text{A}$. The voltage applied to the MCP and the phosphor layer was 0.7 kV and 3.7 kV. The operation mode of the CCD was pixel binning, and the exposure time of the CCD was 1.0 s. The 1D spectrum was obtained by accumulating the lines from 10 to 120 of the 2D spectrum in the vertical direction. The abscissa axis of the 1D spectrum shows the CCD channel. A mass resolution of 130 (10% valley) was achieved at the peak of m/z 18. The expanded 2D spectrum at m/z 18 of Fig. 8 is also shown in Fig. 11(a).

For evaluation of the experimental results, we simulated the 2D spectrum using the transfer matrix method in the second order approximation. The initial position x_0, y_0 and the initial angle α_0, β_0 were set to coincide with the experimental conditions of the main slit; they were chosen in the assumption that ions leaving *via* the main slit would pass through the α -slit. The initial energy spreads of the ions were set from $\delta = -0.001$ to $\delta = 0.001$. These parameters were generated by random numbers using the above initial conditions. The simulated 2D spectrum is shown in Fig. 11(b). The transfer matrix is the one in which the radius of the magnetic field is 50 mm, corresponding to the experimental data shown in Fig. 11(a). The mass resolution of the simulated spectrum is also 130 (10% valley). The experimental result is in good agreement with this simulation.



Fig. 9. 2D spectrum of residual gases.

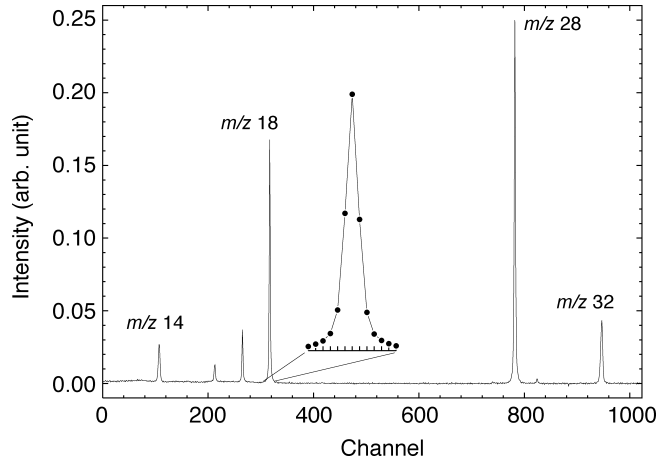
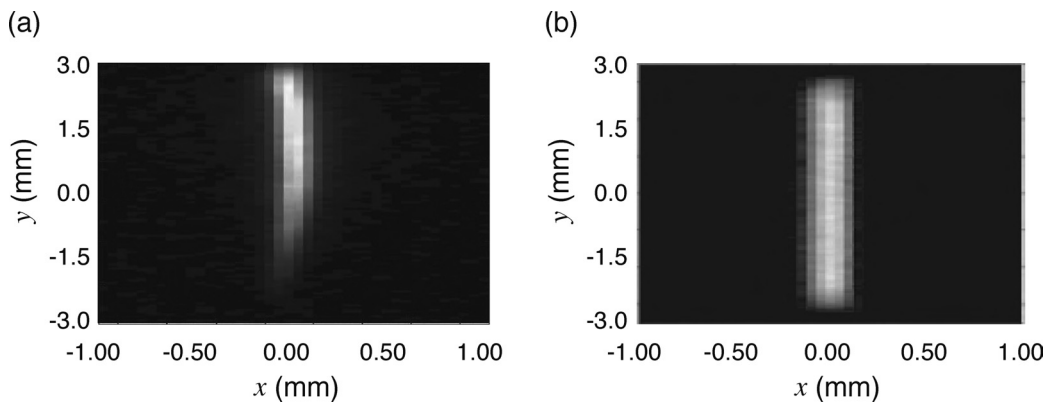


Fig. 10. 1D spectrum of residual gases obtained from the 2D spectrum.

Fig. 11. (a) 2D spectrum expanded around m/z 18 in Fig. 7. (b) Simulated 2D spectrum.

The detectable m/z range depends on the detector size and the detector position. Here, the detector size is about 50 mm; the detectable range varies from 2.5 to 4.4 according to the detector position. In the 1D spectrum of Fig. 10, the detectable m/z range was calculated to be 2.8. This was derived as follows. First, the channel numbers of the abscissa axis were calibrated to m/z . Since m/z is proportional to the square of the mean radius of the ion trajectory in the magnetic sector, the relation between m/z and the channel numbers of the abscissa axis can be expressed as $m/z = ax^2 + bx + c$. Here, a , b , and c denote the calibration coefficients, and x denotes the channel numbers. These coefficients were calculated by applying the least-squares fitting to the channels numbers corresponding to the peak centroids of m/z 14, 18, 28, and 32. In consequence, the 0 and 1024 channels correspond to m/z 12.4 and 34.1, respectively. Next, the detectable range of $34.1/12.4 = 2.8$ was obtained. On the other hand, the mean radius of m/z 34.1 in the magnet is calculated as 68.5 mm when the accelerating voltage and the magnetic flux density are 2200 V and 0.576 T, respectively. When the maximal mean radius in the magnetic field is 68.5 mm, the minimal mean radius is calculated as 41.0 mm by assuming a detector size of 50 mm. The detectable m/z range is then calculated as $(68.5/41.0)^2 = 2.8$. This value is consistent with the experimental result.

The 2D spectra of Kr and Ne were observed to investigate the dynamic range of the detector. The 2D and 1

D spectrum of Kr is shown in Fig. 12. The experimental conditions were as follows: the background pressure was 4.0×10^{-4} Pa in the vacuum chamber and the pressure was increased to 1.3×10^{-3} Pa when Kr gas was introduced; the accelerating voltage of ions was 800 V; the voltage applied to the electrostatic sector was ± 158.4 V; the electron energy and the electron current for ionization were 70 eV and $250 \mu\text{A}$. The voltage applied to the MCP and the phosphor layer was 1.0 kV and 4.0 kV. The operation mode of the CCD was pixel binning and the exposure time of the CCD was 1.0 s. The 2D spectrum shown in Fig. 12(a) is expanded around the spectrum of Kr. The 1D spectrum shown in Fig. 12(b) was obtained by accumulating the lines from 30 to 120 of the 2D spectrum in the vertical direction. All the stable isotopes of Kr are observed simultaneously without saturation of the CCD. Here, the ratios of peak areas were calculated; their peak areas are shown in Table 3. The errors show mean square errors of five consecutive measurements. Each peak area ratio (the roughly estimated isotope ratio) agrees with the standard isotope ratio²⁶⁾ within a deviation of 30%. A dynamic range of 200 was obtained from the $^{78}\text{Kr}/^{84}\text{Kr}$ ratio.

The 1D spectrum of Ne is shown in Fig. 13. The experimental conditions are as follows: the background pressure was 4.0×10^{-4} Pa in the vacuum chamber, and the pressure was increased to 1.3×10^{-3} Pa when Ne gas was introduced; the accelerating voltage of ions

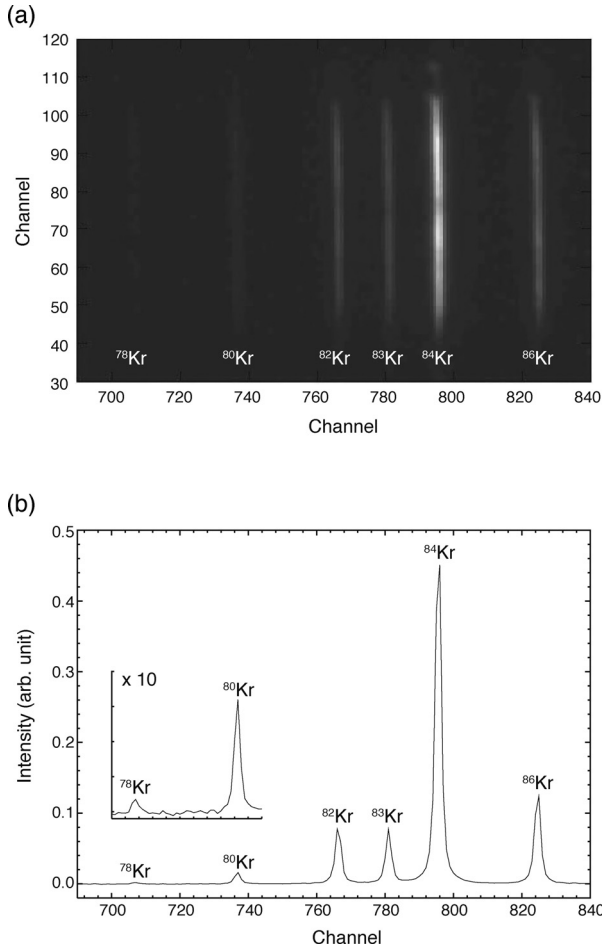


Fig. 12. (a) 2D spectrum of Kr and (b) 1D spectrum of Kr obtained from the 2D spectrum.

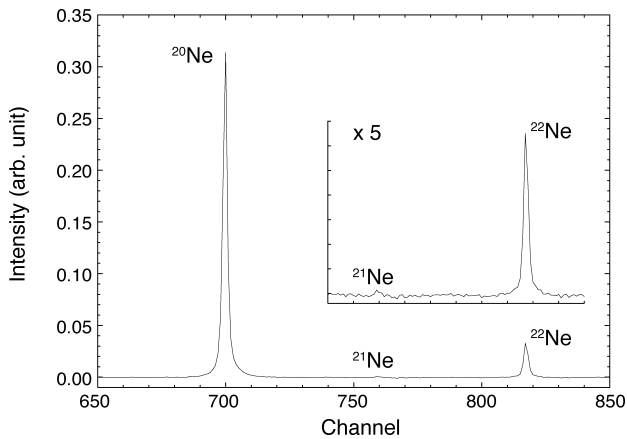


Fig. 13. 1D spectrum of Ne obtained from the 2D spectrum.

was 3050 V; the voltage applied to the electrostatic sector was ± 609.3 V; the electron energy and the electron current for the ionization were 70 eV and 250 μ A. The voltages applied to the MCP and the phosphor layer were 0.9 kV and 4.0 kV. The operation mode of the CCD was pixel binning and the exposure time of the CCD was 1.0 s. The 1D spectrum was obtained by accumulating lines 30 to 120 of the 2D spectrum in the vertical direction. All the stable isotopes of Ne were observed simultaneously without saturation of the

Table 3. Peak Area Ratios of Kr and Ne

	Peak area ratio	Standard isotope ratio
$^{78}\text{Kr}/^{84}\text{Kr}$	0.0041 ± 0.0002	0.0062
$^{80}\text{Kr}/^{84}\text{Kr}$	0.0336 ± 0.0002	0.0401
$^{82}\text{Kr}/^{84}\text{Kr}$	0.173 ± 0.001	0.2034
$^{83}\text{Kr}/^{84}\text{Kr}$	0.156 ± 0.001	0.2018
$^{86}\text{Kr}/^{84}\text{Kr}$	0.276 ± 0.002	0.3032
$^{21}\text{Ne}/^{20}\text{Ne}$	0.0031 ± 0.0003	0.0030
$^{22}\text{Ne}/^{20}\text{Ne}$	0.1087 ± 0.0006	0.1022

CCD, although the signal-to-noise ratio of the ^{21}Ne peak was not sufficient. The ratios of peak areas were calculated. These ratios of peak areas are also shown in Table 3. The errors show mean square errors of five consecutive measurements. These roughly estimated isotope ratios agree with the standard values²⁶⁾ within a deviation of 6%. In addition, a dynamic range of 300 was achieved with the $^{21}\text{Ne}/^{20}\text{Ne}$ ratio.

3. Conclusion

We newly designed and constructed a miniature double focusing mass spectrograph using a focal plane detector as a prototype model for lunar and planetary explorations. We employed the focal plane detector consisting of an MCP, a phosphor layer, a FOP and a CCD. We observed the 2D and 1D spectra of the residual gases, krypton and neon. The experimental value of the mass resolution was in good agreement with the simulation. The experimental value of the detectable m/z range was also consistent with the calculated value. We confirmed that stable isotopes of Kr and Ne could be observed without saturation of the detector. A dynamic range of 300 was achieved experimentally.

References

- 1) A. O. Nier, W. B. Hanson, A. Seiff, M. B. McElroy, N. W. Spencer, R. J. Duckett, T. C. D. Knight, and W. S. Cook, *Science*, **193**, 786 (1976).
- 2) K. Biemann, J. Oro, P. Toulmin, III, L. E. Orgel, A. O. Nier, D. M. Anderson, P. G. Simmonds, D. Flory, A. V. Diaz, D. R. Rushneck, and J. A. Biller, *Science*, **194**, 72 (1976).
- 3) H. B. Niemann, D. N. Harpold, S. K. Atreya, G. R. Carignan, D. M. Hunten, and T. C. Owen, *Space Sci. Rev.*, **104**, 553 (2002).
- 4) H. B. Niemann, W. T. Kasprzak, A. E. Hedin, D. M. Hunten, and N. W. Spencer, *J. Geophys. Res.*, **85**, 7817 (1980b).
- 5) H. B. Niemann, S. K. Atreya, G. R. Carignan, T. M. Donahue, J. A. Haberman, D. N. Harpold, R. E. Hartle, D. M. Hunten, W. T. Kasprzak, P. R. Mahaffy, T. C. Owen, N. W. Spencer, and S. H. Way, *Science*, **272**, 846 (1996).
- 6) K. Birkinshaw, *J. Mass Spectrom.*, **32**, 795 (1997).
- 7) N. S. Belshaw, P. A. Freedman, R. K. O'Nions, M. Frank, and Y. Guo, *Int. J. Mass Spectrom.*, **181**, 51 (1998).
- 8) M. E. Wieser and J. B. Schwieters, *Int. J. Mass Spectrom.*, **242**, 97 (2005).
- 9) C. E. Giffin, H. G. Boettger, and D. D. Norris, *Int. J. Mass Spectrom. Ion Phys.*, **15**, 437 (1974).
- 10) H. H. Tuithof, A. J. H. Boerboom, and H. L. C. Menuzeelaar, *Int. J. Mass Spectrom. Ion Phys.*, **17**, 299 (1975).
- 11) D. Murphy and K. Mauersberger, *Int. J. Mass Spectrom. Ion Processes*, **76**, 85 (1987).

Development of a Miniature Double Focusing Mass Spectrograph

- 12) T. W. Burgoyne, G. M. Hieftje, and R. A. Hites, *J. Am. Soc. Mass Spectrom.*, **8**, 307 (1997).
- 13) M. Ishihara, M. Toyoda, H. Sakae, T. Ichihara, and I. Katakuse, *Environmental Science*, **11**, 15 (2004).
- 14) J. Mattauach and R. Herzog, *Z. Phys.*, **89**, 786 (1934).
- 15) J. Mattauach, *Phys. Rev.*, **50**, 617 (1936).
- 16) H. Yurimoto, K. Nagashima, and T. Kunihiro, *Appl. Surf. Sci.*, **203–204**, 793 (2003).
- 17) J. H. Barnes IV and G. M. Hieftje, *Int. J. Mass Spectrom.*, **238**, 33 (2004).
- 18) T. Sugihara, M. Ohtake, M. Ishihara, M. Toyoda, F. Kunihiro, and M. Shimizu, *J. Mass Spectrom. Soc. Jpn.*, **49**, 69 (2001).
- 19) E. G. Johnson and A. O. Nier, *Phys. Rev.*, **90**, 10 (1953).
- 20) H. Wollnik, "Optics of Charged Particles," Academic Press Inc., London (1987), Chap. 4, p. 104.
- 21) T. Matsuo, H. Matsuda, Y. Fujita, and H. Wollnik, *Mass Spectroscopy (Japan)*, **24**, 19 (1976).
- 22) M. Toyoda and T. Matsuo, *Nucl. Instrum. Methods A*, **427**, 375 (1999).
- 23) K. L. Brown, R. Belbeoch, and P. Bounin, *Rev. Sci. Instrum.*, **35**, 481 (1964).
- 24) H. Wollnik, *Nucl. Instrum. Methods*, **52**, 250 (1967).
- 25) T. Matsuo and H. Matsuda, *Int. J. Mass Spectrom. Ion Phys.*, **5**, 361 (1971).
- 26) J. R. de Laeter, J. K. Böhlke, P. De Bièvre, H. Hidaka, H. S. Peiser, K. J. R. Rosman, and P. D. P. Taylor, *Pure Appl. Chem.*, **75**, 683 (2003).

Keywords: Double focusing mass spectrograph, Focal plane detector, Ion optics